CEAS Aeronautical Journal
https://doi.org/10.1007/s13272-025-00845-y

ORIGINAL PAPER

Experimental investigation of broadband noise generation of a small rotor in hover and forward flight

Felix Lößle[1] · Rainer Schmid[1] · Anna A. Kostek[1] · Daniel Ernst[1] · Clemens Schwarz[1] · Johannes N. Braukmann[1] · C. Christian Wolf[1]

Received: 21 November 2024 / Revised: 4 April 2025 / Accepted: 25 April 2025

Abstract

The mechanisms of sound generation of broadband noise of small rotors are investigated for different flight conditions in an experimental study. A novel microphone array with 512 MEMS microphones is used to investigate the sound emission. Beamforming algorithms are applied to localize the sound generation areas of the broadband noise on the rotor blades. In addition, the optical flow measurement techniques particle image velocimetry and background-oriented schlieren are used to investigate the aerodynamic mechanisms on which the noise is based. The experiments are supplemented by simulations using a panel method. The experiments show that trailing edge noise at 80% of the rotor radius is the dominant sound source mechanism for broadband noise in the frequency range 1–8 kHz in hover. In forward flight, the noise emission depends strongly on the flight condition. When the rotor is tilted against the incoming flow (decelerating maneuver), a C-shaped sound source area occurs in the front of the rotor disk, which can be attributed to interactions of blade tip vortices in the rotor wake with the subsequent rotor blades. In addition, two areas of sound generation on the advancing and retreating rotor side are detected when the rotor is tilted backwards by up to 10°. These are caused by the interaction with the super vortices that form on both sides of the rotor during forward flight.

Keywords Rotor aeroacoustics · Broadband noise · Acoustic beamforming · Background-oriented schlieren · Particle image velocimetry

List of symbols

f_L	Focal length, m
f	Frequency, Hz
Δf	Frequency resolution, Hz
n	Rotational frequency, min^{-1}
PSD	Power spectral density, dB
R	Rotor radius, m
R_A	Beamforming resolution, mm
SPL	Sound pressure level, dB
x_B, y_B	Coordinates in the rotating system, mm
x_R, y_R	Coordinates in the stationary system, mm
v_z	Velocity perpendicular to PIV plane, m/s
V_∞	Inflow velocity, m/s
α	Rotor tilt angle, °
Ψ	Rotor azimuth, °
ω_z	Vorticity, 1/s

✉ Felix Lößle
felixloessle@web.de

[1] DLR, German Aerospace Center, 37073 Göttingen, Germany

1 Introduction

Unmanned aerial vehicles (UAVs) and air taxis with the ability to take off and land vertically are expected to be increasingly used in urban areas. Therefore, their acceptance depends essentially on their noise emissions [1–3]. While the aeroacoustics of helicopters have already been intensively studied, these research results cannot be unrestrictedly applied to multicopters with small rotors. First, multicopters do not require a tail rotor for torque compensation. Second, multicopter are controlled via the rotational frequency of the individual rotors instead of the collective and cyclical pitch angle. Third, the smaller rotors have a more complex blade chord and pitch angle distribution than helicopter rotors. Fourth, multicopter rotors operate at lower Reynolds numbers, altering the aerodynamic characteristics of the airfoils [4–6]. Finally, aerodynamic and acoustic interactions between individual rotors can occur in multicopter configurations.

In recent years, several studies have been published that deal with the investigation of noise emission from small

Published online: 19 May 2025

rotors, both experimentally [7–11] and numerically [12–15]. To investigate the sound generation mechanisms of broadband noise experimentally, acoustic measurements can be combined with optical measurement techniques. One of the few studies involving both acoustic and optical measurements on small rotors was carried out by Grande et al. [16]. They investigated propellers in hover and with axial inflow at Reynolds numbers of 10^4 and were able to detect a laminar separation bubble on the suction side of the rotor using oil-flow visualization and particle image velocimetry (PIV), which led to a high frequency hump in the acoustic spectrum. This sound generation mechanism known as laminar-boundary-layer-vortex-shedding [17, 18] was also observed for small rotors experimentally by Leslie et al. [19] and investigated numerically by Romani et al. [20]. Grande et al. [16] found that turbulence ingestion noise originating at the leading edge of the rotor blades is the dominant broadband noise source in hover. The turbulence impinging the leading edge is caused by the wake of the previous rotor blade.

The influence of turbulence in the rotor inflow on the emission of broadband noise was numerically investigated by Nardari et al. [21] and Thurman et al. [22]. Pettingill and Zawodny [23] experimentally investigated the broadband noise emission of a small rotor in forward flight. They compared the measurements with a broadband noise model [24] developed for helicopter rotors which was fed with numerical simulations of the rotor flow. The investigation showed that the majority of broadband noise for the investigated rotor is created on the advancing side due to trailing edge separation. However, the broadband noise generation mechanisms, especially in forward flight when the flow is complex, are not yet fully understood. Furthermore, it has not yet been investigated whether, under specific flight conditions, the wake and blade tip vortices can interact with the subsequent rotor blades. In the case of blade wakes, this phenomenon is referred to as blade–wake interaction (BWI), which results in broadband noise [25]. In contrast, the interaction of blade tip vortices with subsequent blades, known as blade–vortex interaction (BVI), generates significant tonal noise, with substantial contributions from higher harmonics of the blade passage frequency [26, 27].

Another aeroacoustic effect that contributes to noise emissions in tiltrotor configurations is rotor wake impingement on a wing. This noise generation mechanism was investigated by Chen et al. [28, 29].

In the DLR project "Urban Rescue", the performance, aerodynamics, and acoustics of small rotors operating at low Reynolds numbers are studied. One aim of the project is to investigate the relation between the flow topology and the generation of noise sources to study the sound generation mechanisms. For this purpose, experiments and simulations were conducted on 11 commercial small rotors in hover and various forward flight configurations. The acoustic experiments were performed using a microphone array and acoustic beamforming. The flow topology was investigated using the optical methods background-oriented schlieren (BOS) to visualize the blade tip vortices in the rotor wake and PIV to measure velocity fields in the rotor downwash. The flow around the rotor was simulated using the unsteady free-wake panel method UPM, developed at DLR. This paper presents the results obtained from the acoustic array and the optical methods on a two-bladed rotor, focusing on the investigation of broadband noise generation mechanisms. Selected cases are compared with the results of a three-bladed rotor. The results of the performance measurements are not included in this paper, but can be found in Lößle et al. [30, 31].

2 Experimental setup

The acoustic and optical experiments were carried out at the Rotor Test Facility Göttingen (RTG). A wind tunnel with a nozzle outlet of 0.8 m × 1.6 m provides an edgewise flow with up to 24 m/s into the rotor plane. The nozzle outlet was equipped with Seiferth wings to suppress large-scale shear layer instabilities [32]. The velocity was measured with a Prandtl probe in the nozzle outlet. As shown in Figs. 1, 2, 3 and 4, the rotor was installed on a shaft mounted horizontally in the center of the test section. The rotor was driven by a brushless DC motor with a maximum power of 180 W. The rotational frequency was measured with an encoder on the motor shaft and deviated from the target frequency by less than 0.05%. The drive unit was mounted on a rotatable support system allowing the tilt angle of the rotor to be varied between −30° (rotor tilted in the direction of the flow) and +30° (rotor tilted backwards). To minimize

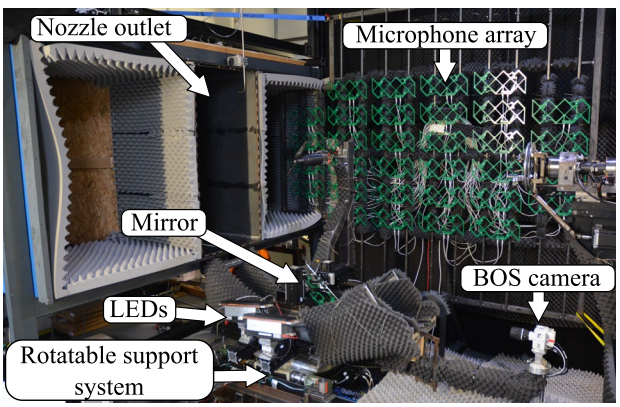

Fig. 1 Setup of the BOS and microphone array measurements in the RTG

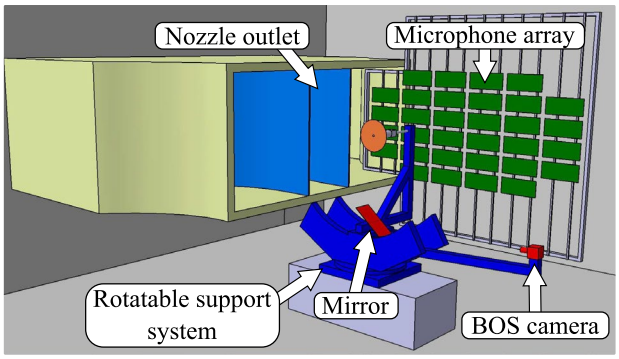

Fig. 2 Model representation of the experimental setup

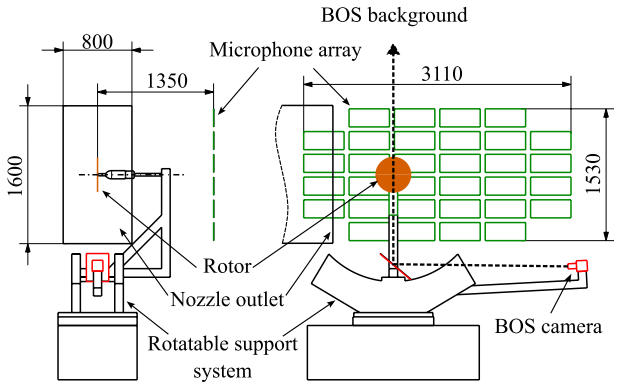

Fig. 3 Sketch of the microphone array and BOS setup

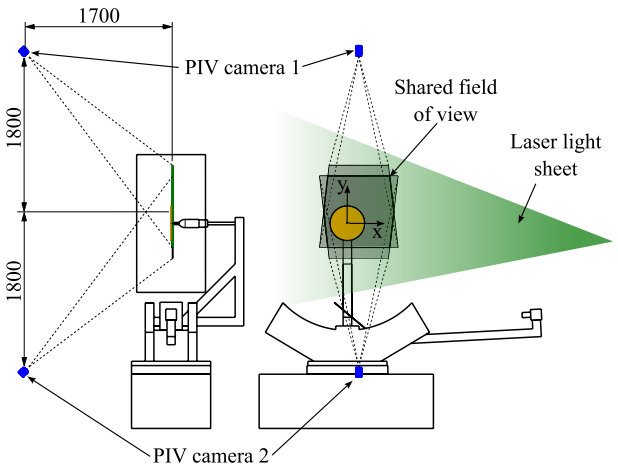

Fig. 4 Sketch of the PIV setup

aerodynamic interference, the drive unit was covered with an aerodynamic fairing.

A total of 11 commercial 2- and 3-bladed rotors with rotor radii between 15.3 cm and 23.5 cm were examined in the campaign. This paper shows results obtained with the two-bladed rotor CAMcarbon Light 16 × 6 from Aeronaut ($R = 0.203$ m) and with the three-bladed rotor CF125-TP from KDE Direct ($R = 0.159$ m). The CAMcarbon Light 16 × 6 rotor is a rigid rotor, while the rotor head of the CF125-TP rotor allows lead-lag motion.

2.1 Acoustic measurements

The acoustic measurements were carried out with a planar microphone array consisting of 512 microelectromechanical (MEMS) microphones distributed on 32 identical circuit boards with 16 microphones each (see Fig. 20 in Appendix). The ICS-52000 microphones from InvenSense with integrated 24-bit AD converter have a usable frequency range between 50 Hz and 20 kHz, a sensitivity deviation of ±1 dB. They were read out time-synchronized at a sampling frequency of 32 kHz using a field programmable gate array (FPGA). A more detailed description of the technical operating principle of a similar microphone array with the same hardware architecture can be found in Ernst et al. [33]. As shown in Fig. 3, the microphone array was mounted parallel to the rotor plane at a distance of 1350 mm. The microphone array has a length of 3110 mm in the flow direction and a width of 1530 mm in the spanwise direction. The sound emitted by the rotor was recorded over a duration of 20 s for each measurement. The position of the microphone array was calibrated acoustically using a piezoelectric loudspeaker. For this purpose, white noise emitted by the loudspeaker at different positions in the rotor plane was recorded by the microphone array and evaluated using beamforming. The spatial resolution of the microphone array defined as the 3 dB main lobe width of a single point source was determined based on calibration measurement and theoretical estimates according to Sijtsma [34]. For the used microphone array, the resolution is $R_A = 15$ mm at a frequency of 12 kHz.

The acoustic measurements were not carried out in an acoustic wind tunnel. Although the rotatable support system and the wall of the plenum behind the microphone array were covered with acoustic absorbers, the reflection of sound could not be completely avoided. The superposition of the incident sound wave with the reflected sound wave increased the measurement uncertainty of the sound pressure levels at the microphones of the array. For this reason, the influence of reflections must be considered in the quantitative evaluation when conducting measurements with single microphones in this measurement setup. In contrast, the source maps calculated using beamforming are not affected by the reflections as the reflected component can be separated from the directly received component due to the time delay.

Acoustic beamforming is used to localize the sound generation areas of the broadband noise emitted by the rotor.

Two approaches, differing in the choice of points on which the array is focused, were taken to calculate the source areas. First, the microphone array was focused on stationary focus points in the rotor plane. This choice of focus points was used to investigate where the broadband noise is generated on the rotor disk. The Conventional Beamforming algorithm as described in Sijtsma [34] was used for this purpose. Second, the microphone array was focused on focus points that corotate with the rotor to indicate where the noise is generated at the rotor blades. The applied Rotating Source Identifier (ROSI) algorithm is described in detail in Sijtsma et al [35].

2.2 Background-oriented schlieren

Background-oriented schlieren (BOS) is an optical measurement technique used to detect refractive index gradients in the flow field [36]. Since the blade tip vortices of rotors generate density inhomogeneities and thus fluctuations in the refractive index in the flow field, the measurement technique is suitable for the qualitative detection of blade tip vortices in the rotor wake [37]. For BOS, two images of a high-contrast background are taken with a camera: with the rotor under investigation between the camera and the background (measurement image) and without the rotor (reference image). The density inhomogeneities in the rotor wake caused by the blade tip vortices lead to a local shift in the background pattern which can be visualized by cross-correlating the two images.

A retroreflective foil printed with a random dot pattern (diameter 1 mm) was attached to the ceiling of the wind tunnel as a background and was illuminated with four LED spotlights. A Phantom VEO 640 L camera (specifications see Table 1 in Appendix) was mounted on a cantilever arm of the rotatable support system to provide a lateral perspective of the rotor independent of the rotor tilt angle under investigation. As shown in Figs. 2 and 3 the camera was focused on the background via a mirror below the rotor. The optical path between background and rotor as well as between rotor and camera was 2.9 m. The DaVis software from LaVision was used to evaluate the images based on correlation. A total of four iterations with decreasing window sizes were carried out. In the first iteration, a round Gaussian-weighted evaluation window with dimensions of 48 px × 48 px and an overlap of 50% was used; in the last iteration, a round Gaussian-weighted window with dimensions of 16 px × 16 px and an overlap of 75% was used.

Figure 5 shows the result of the correlation for the rotor CAMcarbon Light 16 × 6 in hover. The helical blade tip vortex system of the rotor can be observed in the rotor wake. To evaluate the trajectories of the blade tip vortices, the outermost vortex positions are extracted for all images, as marked in the figure.

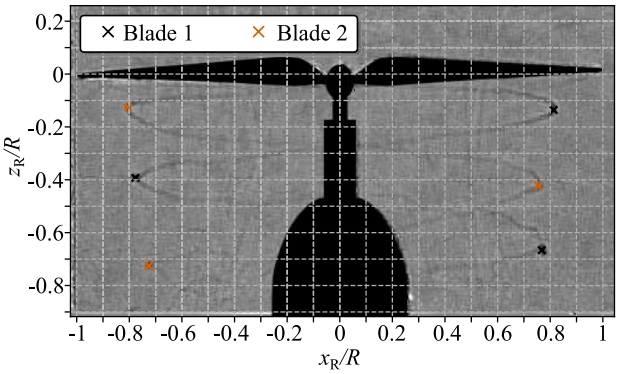

Fig. 5 Visualization of the vortex system with BOS of the rotor CAMcarbon Light 16 × 6 in hover at a rotational frequency of $n = 4000\,\mathrm{min}^{-1}$

2.3 Particle image velocimetry

The flow field under the rotor was examined using stereoscopic particle image velocimetry (PIV). For this purpose, the plane parallel to the rotor disk and 14 mm below the rotor was illuminated with two Quantel EverGreen 200 Nd:YAG dual cavity lasers, each with a pulse energy of 200 mJ. Near the inlet of the wind tunnel, di-ethyl-hexyl-sebacate (DEHS) oil droplets serving as flow tracers were fed into the flow using two PIVcts1000 and two PIVpart45 seeding generators. The first generator type produced droplets with an average diameter of 2 µm, while the latter produced droplets with an average diameter of 0.9 µm. Two PCO.edge 5.5 CMOS cameras (specifications see Table 1 in Appendix) were used for image acquisition. As shown in Fig. 4, the cameras were positioned at a distance of 1700 mm from the light sheet and each recorded the light sheet at an angle of 43°. Double images with a time offset of $\Delta t = 80\,\mu\mathrm{s}$ were recorded. The stereoscopic camera system was calibrated using a 3D calibration plate with a dot pattern (LaVision Type 31) before the measurement.

The software DaVis from LaVision was used for the correlation-based evaluation of the images. A total of four iterations with decreasing window size were carried out. In the first iteration, an unweighted quadratic evaluation window with the dimensions 48 px × 48 px and an overlap of 50% was used; in the last iteration, a round Gaussian-weighted window with the dimensions 16 px × 16 px and an overlap of 75% was used. These settings resulted in a resolution of the velocity field of 1.19 mm. Areas of the light sheet that were blocked from the cameras' view due to the rotor blades were masked in the post-processing.

2.4 Unsteady panel method

The unsteady panel method (UPM) developed by DLR was used to simulate the rotor aerodynamics [38, 39]. The displacement effect of the rotor blades is modeled using a discrete source and sink distribution on the blade surface. The strength of the sources and sinks is computed in each calculation step so that the kinematic boundary condition on the rotor surface is fulfilled. The lift is modeled using a vortex distribution on the camber line of the rotor blade. The trailing edge of the airfoil is closed with a Kutta panel to prevent a flow around the trailing edge (fulfillment of the Kutta condition). UPM uses a non-linear, unsteady wake model for the rotor wake. The rotor wake is modeled using point-shaped vortex particles [40]. In each calculation step, a new vortex particle is released from the trailing edge behind each spanwise rotor segment and added to the wake. The velocity induced by the vortex particles influences both the inflow of the rotor blades and the movement of the vortex particles in the rotor wake. To take into account the viscous forces in the boundary layer, viscous corrections are applied to the forces acting on the rotor blades in post-processing. The Eppler method [41] was used to calculate the laminar and turbulent boundary layers and the e^n method by Drela and Giles [42] was used to estimate the transition. A validation of the code for small rotors and multicopters was conducted by Kostek et al. [12, 43].

The blade model is based on a 3D scan of the rotor. The scans were used to determine the airfoil, chord length, and pitch angle at 20 blade sections along the span. Based on the geometry data, the surface was segmented into 15 panels along the span and 95 panels along the blade chord. To take the influence of the cover of the drive unit into account, the cover model was integrated into the UPM model as a blunt body.

The calculated thrust and torque converged after ten rotations. An initial step size of 5° rotor azimuth was selected for the first four rotations and was then reduced to 2° rotor azimuth.

3 Results in hover

Figure 6 shows the power density spectrum of the CAMcarbon Light 16 × 6 rotor in hover as well as the spectrum of the background noise and the motor. The spectra were recorded with one of the microphones of the microphone array located outside the rotor downwash ($x = 0,017$ m, $y = 0,764$ m, $z = -1,35$ m). The comparison between the two spectra shows that the rotor noise dominates the spectrum in the entire frequency range. As already mentioned, the experiment was carried out in an acoustically uncovered wind tunnel and the spectrum can only be interpreted

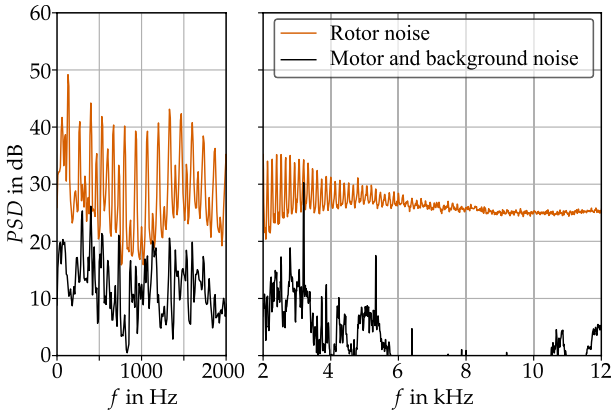

Fig. 6 Power density spectrum *PSD* of the CAMcarbon Light 16 × 6 rotor in hover at a rotational frequency of $n = 4000\,\mathrm{min}^{-1}$, frequency resolution $\Delta f = 10$ Hz, microphone location: $x = 0,017$ m, $y = 0,764$ m, $z = -1,35$ m

qualitatively due to reflections from the walls of the plenum. The highest sound emission occurs at the blade passing frequency of the rotor ($f = 133$ Hz). Higher harmonics of the blade passing frequency occur up to a frequency of 6 kHz with a tendency to decrease in level with increasing order. In addition, up to a frequency of 2 kHz, harmonics of the rotor rotational frequency occur between the higher harmonics of the blade passing frequency, which are not to be expected under ideal operating conditions for rotors in hover. These are due to asymmetries in the connection of the rotor to the rotatable support system. Furthermore, a recirculation flow forms in the plenum during hover, which leads to an uneven inflow into the rotor and can result in the occurrence of harmonics of the rotational frequency. At higher frequencies, the noise emitted by the rotor is dominated by broadband noise.

In the following, the broadband noise emitted by the rotor is investigated using beamforming. The resulting acoustic source maps are shown in Fig. 7 for the three octave bands between 1 kHz and 8 kHz both in the rotating (a–c) and in the stationary (d–f) reference system of the beamforming focal points. As the resolution of the microphone array decreases at lower frequencies, the source areas at lower frequencies become increasingly blurred. The source maps in the rotating system show that the broadband noise in all three investigated octave bands is mainly generated at the trailing edge at about 80% of the rotor radius, and thus trailing edge noise is the dominant noise generation mechanism in these frequency ranges. This is emphasized by Fig. 8, which illustrates the position of the maximum of the three octave bands for a rotational frequency of $3000\,\mathrm{min}^{-1}$ and $4000\,\mathrm{min}^{-1}$. Aerodynamic simulations with UPM show that the radial position of the maximum noise emission coincides with the position of maximum lift generation on

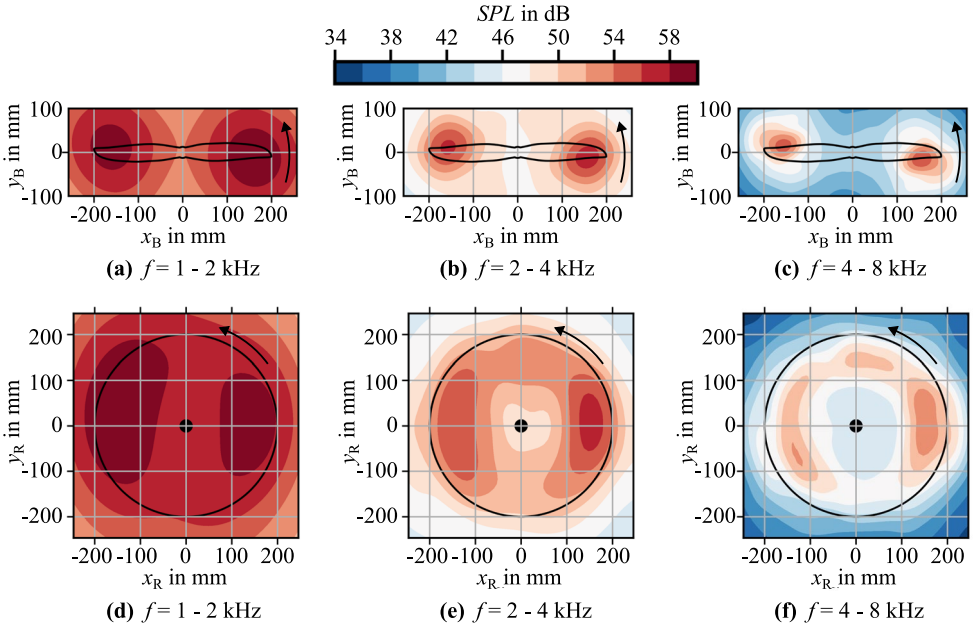

Fig. 7 Acoustic source maps in the rotating reference system (**a**–**c**) and in the stationary reference system (**d**–**f**) of the CAMcarbon Light 16 × 6 rotor in hover at a rotational frequency of $n = 4000\,\mathrm{min}^{-1}$

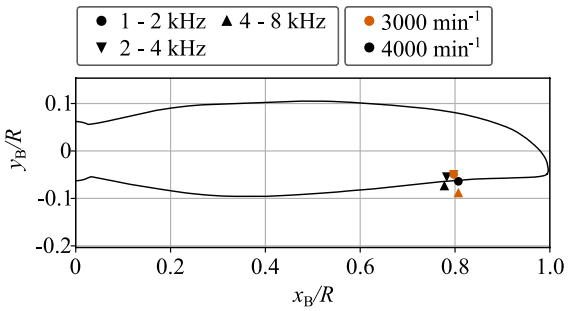

Fig. 8 Position of the maximum sound emission on the rotor blade of the CAMcarbon Light 16 × 6 rotor in hover

the rotor blade. For comparison, Fig. 9 shows the acoustic source maps for the three octave bands of the three-bladed KDE Direct CF124-TF rotor at a rotational frequency of 5650 min^{-1}. The position of the maximum noise emission for this three-bladed rotor is also located at the trailing edge of the rotor blades at 80% of the rotor radius.

As shown in Fig. 7d–f, the sound generation area that is stationary at the trailing edge of the airfoil in the rotating reference system appears as an annular in the stationary reference system. Under undisturbed conditions, a rotationally symmetric distribution of the source strength is expected. However, the experimentally determined distribution depends on the rotor azimuth for all octave bands investigated. This is due to the previously mentioned asymmetry of the mechanical connection of the rotor to the rotatable support system and the formation of flow recirculation in the plenum.

Next, the relation between the sound pressure level of the dominant broadband noise source on the rotational frequency is investigated. For this purpose, measurements were taken in the rotational frequency range between 3000 min^{-1} and 4000 min^{-1} with a step size of 200 min^{-1} (two measurements per rotational frequency) and the

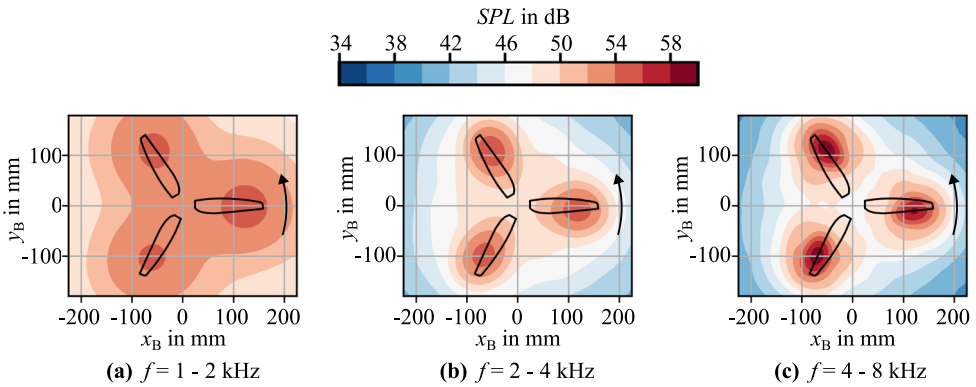

Fig. 9 Acoustic source maps in the rotating reference system of the rotor KDE Direct CF125-TP rotor in hover at a rotational frequency of $n = 5650\,\mathrm{min}^{-1}$

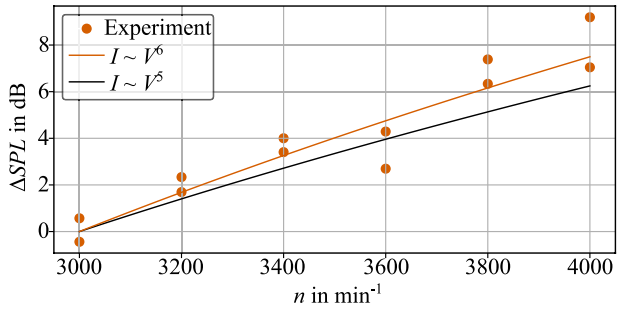

Fig. 10 Dependence of the sound pressure level *SPL* for the frequency range 1–8 kHz of the dominant broadband sound source at the trailing edge of the blade at 80% of the rotor radius on the rotational frequency n; CAMcarbon Light 16 × 6 rotor in hover

sound pressure levels at the trailing edge of the rotor at 80% of the rotor radius for the frequency range 1–8 kHz are extracted from the source maps. Figure 10 shows the level differences relative to the measurement at a rotational frequency of 3000 min^{-1}. While according to the theoretical model of Ffowcs Williams and Hall [44], a dependence of V^5 would be expected, the measurements rather show a proportionality of the intensity with the local flow velocity V^6.

4 Results in forward flight

Longitudinal inflow to the rotor significantly influences the rotor flow field, vortex dynamics, and aeroacoustics, with these effects mainly depending on the flow velocity and the rotor tilt angle. To investigate the effects, experiments were conducted for the CAMcarbon Light 16 × 6 rotor at a rotational frequency of 4000 min^{-1} with inflow velocities varying between 4.4 m/s and 23.2 m/s, resulting in advance ratios μ between 0.05 and 0.28, and rotor tilt angles between −30° and +30°. Figure 11 shows the acoustic source maps calculated with non-rotating focus points for the investigated operating conditions for the octave band 4–8 kHz. Owing to the power limitation of the motor, measurements could not be performed for combinations of high inflow velocities and large

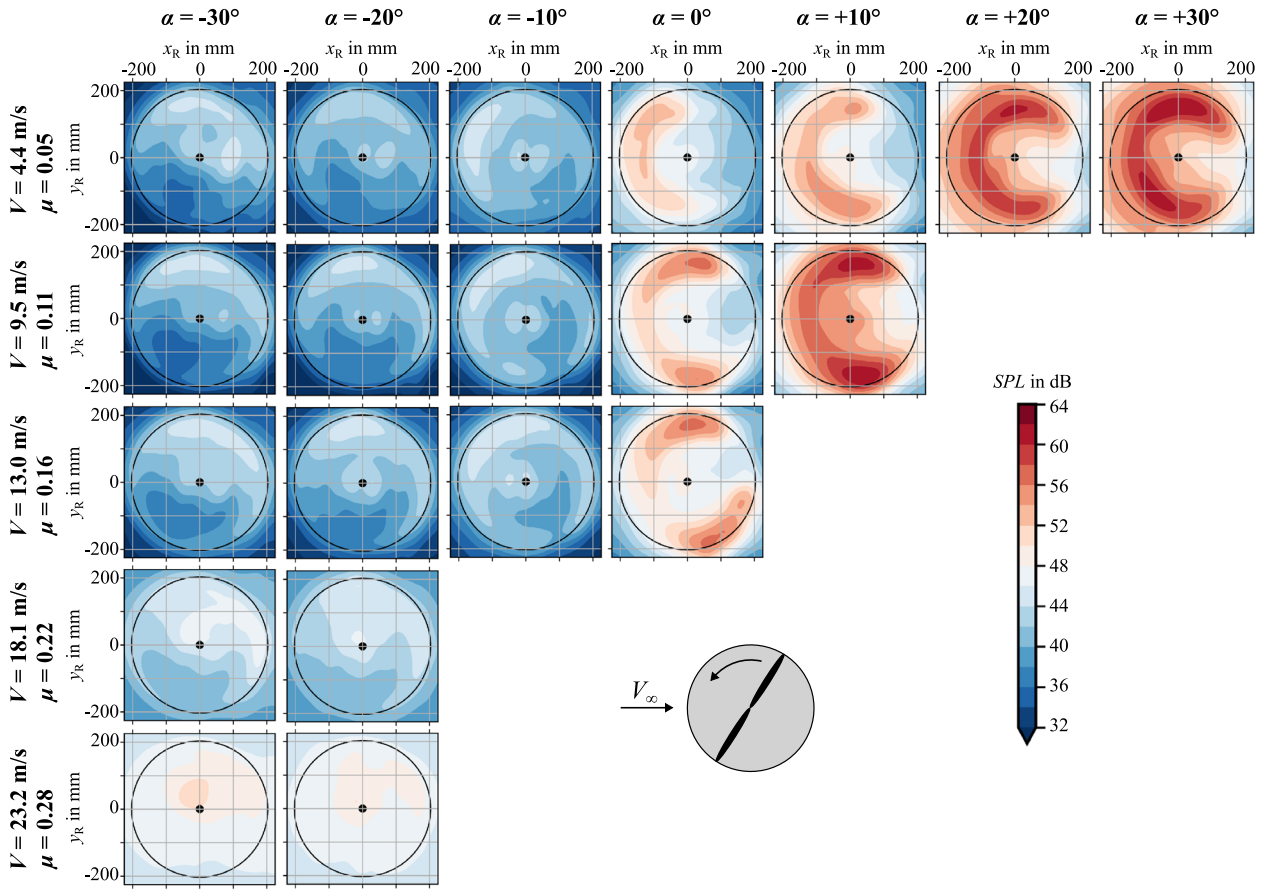

Fig. 11 Acoustic source maps in the stationary reference system of the CAMcarbon Light 16 × 6 rotor in forward flight at a rotational frequency of n = 4000 min^{-1}, varying inflow velocity V_∞, advance ratio μ and tilt angle α for the octave band 4–8 kHz

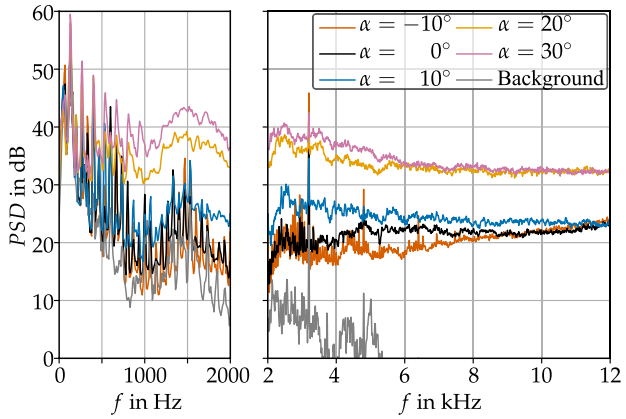

Fig. 12 Power density spectrum PSD of the CAMcarbon Light 16 × 6 rotor in forward flight at a rotational frequency of $n = 4000\,\mathrm{min}^{-1}$, an inflow velocity of $V_\infty = 4.4\,\mathrm{m/s}$ ($\mu = 0.05$) and varying tilt angles α, frequency resolution $\Delta f = 10\,\mathrm{Hz}$, microphone location: $x = 0,017$ m, $y = 0,764$ m, $z = -1,35$ m

positive tilt angles. The source maps indicate that the sound emission on the advancing rotor side tends to be higher than on the retreating rotor side due to the higher relative flow velocities. Furthermore, they reveal a strong dependency of the noise emission of the inflow velocity and the rotor tilt angle: as the rotor tilt angle increases, a C-shaped sound generation region forms in the front area of the rotor disk. Moreover, an increase in inflow velocity at tilt angles of 0° and +10° results in enhanced sound emission on both the advancing and retreating sides of the rotor. In the following, the sound generation mechanisms underlying these two effects are analyzed separately. The results from the BOS and PIV experiments, along with simulations using UPM, are used to elucidate the aerodynamic effects responsible for sound generation.

4.1 Effect of tilt angle

Figure 12 illustrates the influence of the tilt angle on the power density spectrum of the emitted sound for an inflow velocity of 4.4 m/s ($\mu = 0.05$). The rotor tilt angle affects both the tonal and the broadband components of the emitted sound. The highest sound emission is observed for all tilt angles at the blade passing frequency of the rotor. With an increase in tilt angle, the sound pressure level of the harmonics of the blade passing frequency increases by up to 15 dB. The sound pressure level of the broadband noise also increases with growing tilt angle, with the greatest increase occurring when the tilt angle is increased from 10° to 20°. This suggests that the flow around the rotor blades undergoes a qualitative change between these two tilt angles.

To further investigate the influence of the tilt angle on broadband noise emission, the acoustic source maps for the octave band 4–8 kHz are shown in Fig. 13. For tilt angles of 0° and higher, broadband noise is predominantly emitted in the front area of the rotor disk. As the tilt angle increases, the region of sound generation expands, forming a C-shaped area.

Figure 14 shows the acoustic source maps in the rotating reference system for the octave band 4–8 kHz. For all investigated tilt angles, the dominant sound sources are located at the trailing edge of the rotor blades, similar to hover conditions. Regarding the radial location, the sound sources at a tilt angle of −10° are positioned at 80% of the rotor radius, as observed in hover. As the tilt angle increases, the dominant sound source gradually shifts inwards to approx. 70% of the rotor radius.

The BOS experiments are used to investigate the aerodynamic phenomena responsible for the sound generation mechanisms. Figure 15 depicts the trajectories detected

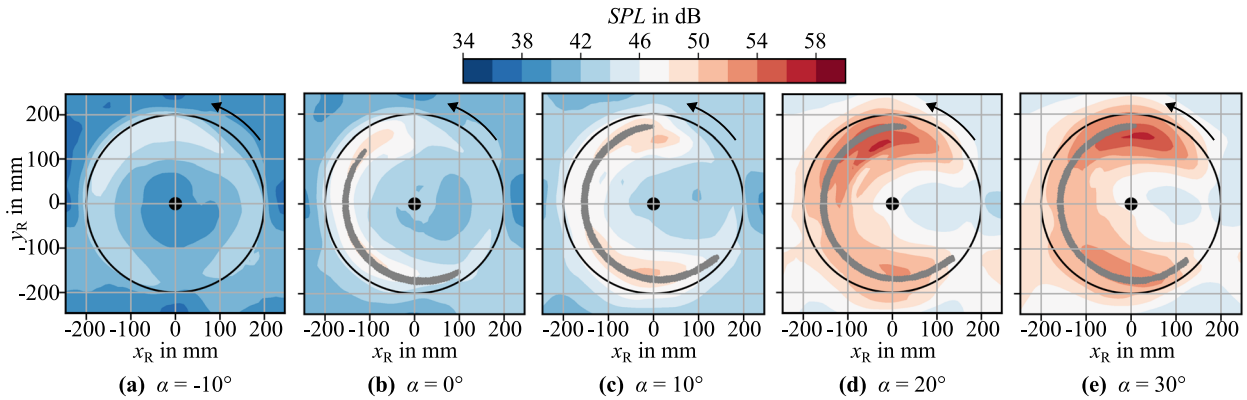

Fig. 13 Acoustic source maps in the stationary reference system of the CAMcarbon Light 16 × 6 rotor for the octave band 4–8 kHz in forward flight at a rotational frequency of $n = 4000\,\mathrm{min}^{-1}$, an inflow velocity of $V_\infty = 4.4\,\mathrm{m/s}$ ($\mu = 0.05$, flow from left to right) and varying rotor tilt angle α. The positions of the blade tip vortices in the rotor plane determined with UPM are shown in gray

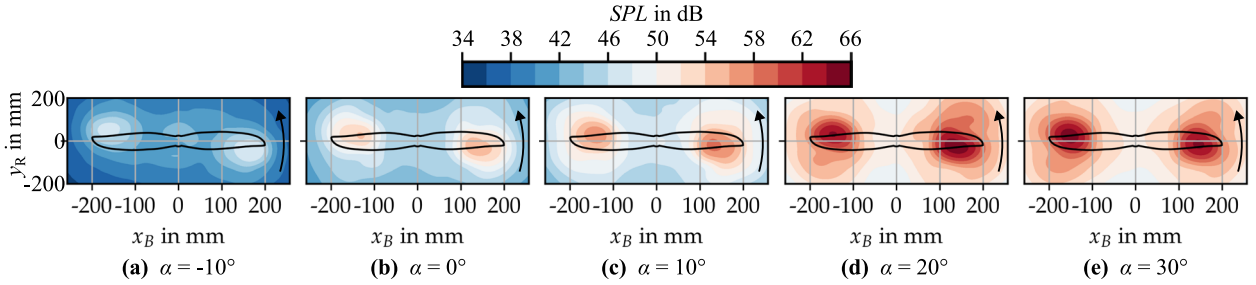

Fig. 14 Acoustic source maps in the rotating reference system of the CAMcarbon Light 16 × 6 rotor for the octave band 4–8 kHz in forward flight at a rotational frequency of $n = 4000\,\mathrm{min}^{-1}$, an inflow velocity of $V_\infty = 4.4\,\mathrm{m/s}$ ($\mu = 0.05$) and varying rotor tilt angle α

from the BOS images of the blade tip vortices, which originate at the front and rear ends of the rotor. When the rotor is tilted forward ($\alpha < 0°$), the blade tip vortices generated at the front of the rotor move downwards, away from the rotor plane, due to the inflow component perpendicular to the rotor plane and the velocity induced by the rotor. As the subsequent blade passes, an additional velocity component perpendicular to the rotor plane is induced on the blade tip vortex, resulting in a kink in the vortex trajectory. With increasing rotor tilt angle, the downward flow component is reduced, leading to a reduction in the distance between the vortex trajectories and the rotor plane. At a rotor tilt angle of 20° or greater, the blade tip vortices remain within the rotor plane or are located just above the rotor plane immediately after their formation. Under there conditions, the blade tip vortex interacts with the subsequent rotor blade and is destroyed in the process.

The position of BVI detected with BOS is located at approx. 70% of the rotor radius and corresponds to the position of the noise source in the acoustic source maps in the stationary reference system, along the center axis where $y_R = 0$ mm. It also explains the observed inward shift of the sound sources in the source maps of the rotating reference system, which occurs for increasing tilt angles.

With BOS, only the two-dimensional projection of the three-dimensional vortex structure can be displayed. UPM simulations are performed to obtain three-dimensional information about the vortex system. The positions of the blade tip vortices in the rotor plane, as simulated with UPM, are marked in gray in addition to the acoustic source maps in Fig. 13. These indicate the locations where BVI is expected. The comparison with the acoustic source maps shows good agreement with the broadband noise source. This demonstrates that the C-shaped noise source area is a result of BVI.

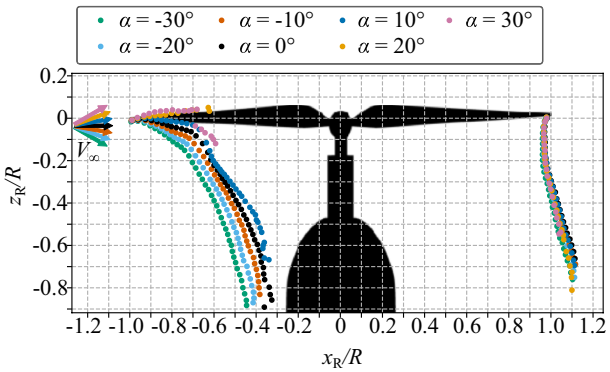

Fig. 15 Impact of the rotor tilt angle α on the trajectory of the blade tip vortices of the CAMcarbon Light 16 × 6 rotor at a rotational frequency of $n = 4000\,\mathrm{min}^{-1}$ and an inflow velocity of $V_\infty = 4.4\,\mathrm{m/s}$ ($\mu = 0.05$)

4.2 Effect of flow velocity

In addition to the tilt angle, the rotor noise emission is also influenced by the flow velocity. Particularly, when the velocity increases at a rotor tilt angle of 10°, the sound emission on the advancing and retreating rotor side rises, which will be examined in the following.

Figure16 illustrates the effect of the flow velocity on the power density spectrum of the sound emitted by the CAMcarbon Light 16 × 6 rotor at a tilt angle of 10°. The broadband noise of the rotor increases across the entire frequency range investigated as the inflow velocity rises. The increase in broadband noise does not proceed uniformly with the increase in incident flow velocity: while the broadband noise increases by up to 17 dB (depending on the frequency) from 4.4 m/s to 7.8 m/s ($\mu = 0.05 - 0.09$), the increase in velocity between 7.8 m/s and 9.5 m/s ($\mu = 0.09 - 0.11$) leads to a significantly weaker increase with a maximum of 2 dB.

The acoustic source maps of the rotor for a tilt angle of 10° and the varying velocities examined are shown in Fig. 17a–c. In the front rotor area, the source maps reveal the

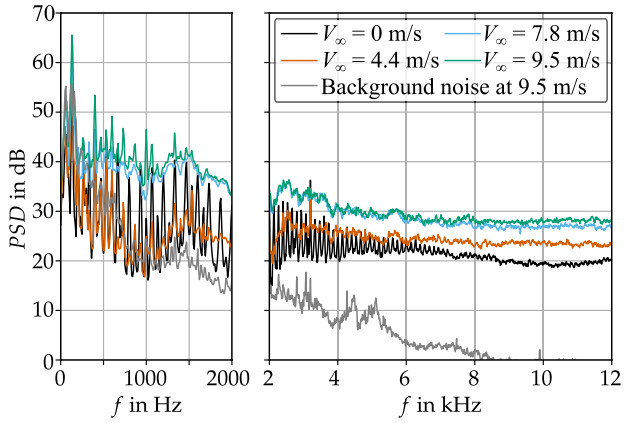

Fig. 16 Power density spectrum *PSD* of the CAMcarbon Light 16 × 6 rotor in forward flight at a rotational frequency of $n = 4000\,\mathrm{min}^{-1}$, a tilt angles of $\alpha = 10°$ and varying inflow velocities V_∞, frequency resolution $\Delta f = 10\,\mathrm{Hz}$, microphone location: $x = 0,017$ m, $y = 0,764$ m, $z = -1,35$ m

C-shaped sound generation areas discussed earlier, which can be attributed to BVI. In addition, when the velocity increases from 4.4 m/s to 7.8 m/s ($\mu = 0.05 - 0.09$), two prominent sound generation areas emerge on the advancing and retreating sides of the rotor. With a further increase of the inflow velocity to 9.5 m/s ($\mu = 0.11$), there is no significant change in sound emission.

PIV measurements and UPM simulations are performed for an inflow velocity of 12.7 m/s ($\mu = 0.15$) and the two rotor tilt angles of 10° and −10° to identify the aerodynamic effect that leads to the generation of the two sound sources on the advancing and retreating rotor side. A reference will be made again to the acoustics after the discussion of the flow field.

Figure 18a, b depicts the flow field of the rotor captured with PIV in the light sheet 14 mm below the rotor. The colors represent the velocities v_z perpendicular to the PIV plane, the velocity components in the plane are represented by vectors. The projection of the rotor disk onto the PIV plane is illustrated by a circle. At a tilt angle of −10°, the stream tube of the rotor downwash clearly stands out from the external flow field. Due to the longitudinal inflow, the center of the stream tube is shifted downstream relative to the rotor axis. The blade tip vortices, which represent the boundary between the stream tube and the external flow, are clearly visible in the flow field. In contrast, the rotor wake for a tilt angle of +10° does not exhibit a clear boundary between the stream tube and the outer flow; instead, a stretched downwind field of the rotor can be seen. Due to the higher relative velocities on the rotor blade and the associated higher lift on the advancing rotor side than on the retreating rotor side, the downwash velocity on the advancing side exceeds that on the retreating side. Laterally next to

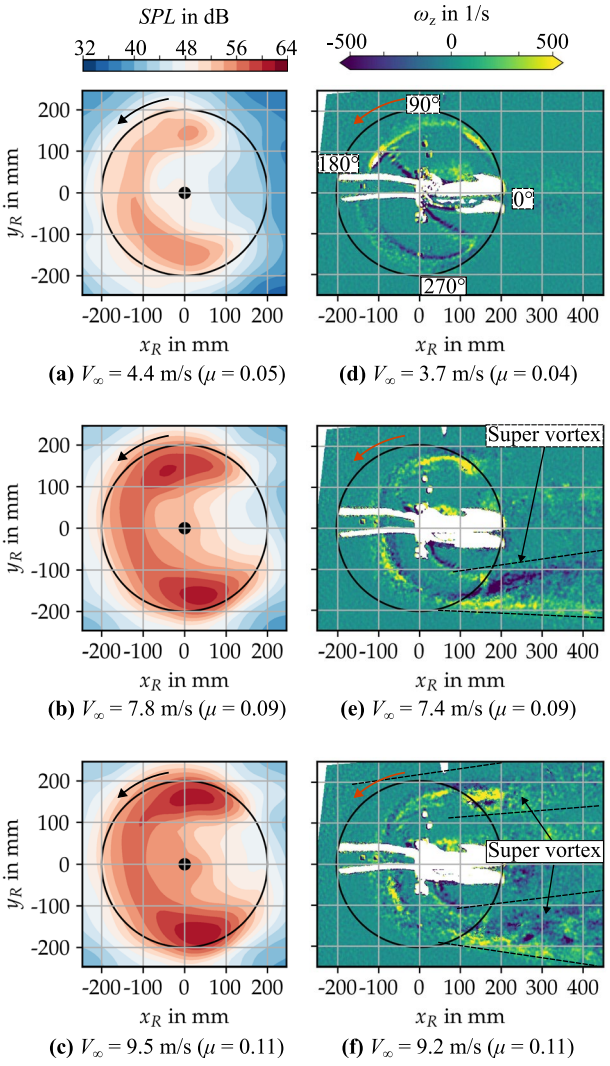

Fig. 17 Acoustic source maps for the octave band 4–8 kHz (**a**–**c**) and vorticity of the velocity field (**d**–**f**) of the rotor CAMcarbon Light 16 × 6 in forward flight at a rotational frequency of $n = 4000\,\mathrm{min}^{-1}$, a rotor tilt angle of $\alpha = 10°$ and varying flow velocities V_∞.

the downwash field, the flow field has an area with positive, upward velocities.

The velocity field simulated with UPM illustrated in Fig.18c, d shows good agreement with the flow field of the rotor measured with PIV. In addition, the figure shows the simulated vortex particles in the rotor wake. Figure 19 displays the vortex system viewed against the direction of the incident flow as well as the position of the rotor plane and light sheet. The side views reveal that the vortex particles generated by the two rotor blades rapidly descend below the rotor plane at a tilt angle of −10°, whereas at a tilt angle of +10°, the vortex particles stay close to the rotor plane. The blade tip vortices, which form laterally on the advancing and retreating sides of the rotor, roll up into conical super vortices that are similar to the wake vortices of fixed-wing aircraft. They account for the upwind observed laterally next to

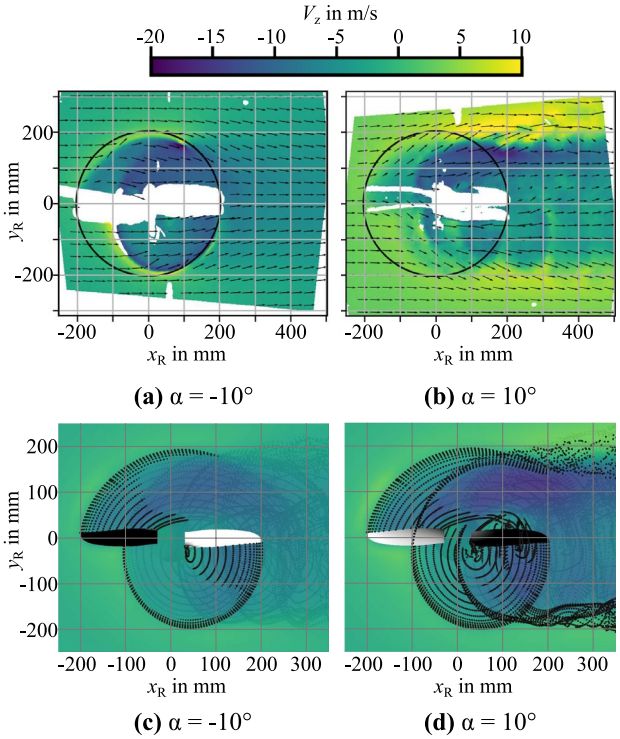

Fig. 18 Velocity field of the rotor CAMcarbon Light 16 × 6 measured with PIV (**a**-**b**) and calculated with UPM (**c**-**d**) at a rotor azimuth of $\Psi = 0°$, an inflow velocity of $V_\infty = 12.7\,\mathrm{m/s}$ ($\mu = 0.15$), and a rotor tilt angle of $\alpha = -10°$ and $\alpha = 10°$. Vortex particles of the rotor wake are visualized by dots in the UPM results

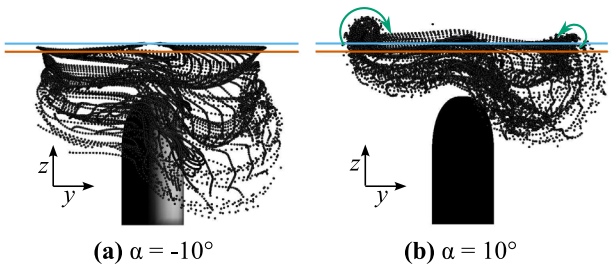

Fig. 19 Vortex structure of the rotor wake simulated with UPM at an inflow velocity of $V_\infty = 12.7\,\mathrm{m/s}$ ($\mu = 0.15$) and a rotor tilt angle of $\alpha = -10°$ and $\alpha = 10°$. View against the flow direction. The rotor plane (—) and the light sheet plane (—) are also shown

the rotor downwash. The super vortex on the retreating side has a larger diameter than the super vortex on the advancing side. Due to the higher lift and the resulting higher downwash velocity on the leading side, the tip vortex is lower on the advancing side. Such a roll up of the blade tip vortices on the sides of a rotor was also observed experimentally by smoke visualizations by Ghee and Elliott [45] and numerically by Tan and Wang [46].

Due to the position of the sound generation areas on the advancing and retreating rotor sides, it is reasonable to assume that these are associated with the generation of the super vortices. To investigate this relation in more detail, the acoustic source maps at a rotor tilt angle of +10° and varying inflow velocity are compared with the results from the PIV measurement in Fig. 17. The visualization of the vortex structures in the PIV measurements is carried out using the vorticity. The flow field for 3.7 m/s ($\mu = 0.04$) shows blade tip vortices behind the two rotor blades. The shear layers forming behind the rotor blades can be seen approximately 45° behind the two blades. When the inflow velocity is increased to a velocity of 7.4 m/s ($\mu = 0.09$), the PIV measurements show that the blade tip vortices roll up to super vortices initially on the retreating side. If the velocity is further increased, the blade tip vortices also begin to roll up to super vortices on the advancing side. The roll up begins in the area of the rotor disk at a rotor azimuth of 50° –90° on the advancing side and 290°–320° on the retreating side. The position of the beginning roll up of the tip vortex corresponds well with the position of the sound generation areas on the advancing and retreating rotor side. This indicates that the super vortices carry older blade tip vortices from the rotor wake back into the rotor plane and are responsible for the acoustic source areas on the advancing and retreating rotor side.

5 Conclusion

Acoustic wind tunnel experiments were carried out with a microphone array to investigate the sound emission of small rotors. Beamforming was used to detect acoustic broadband sources in the rotor disk from the microphone array measurements. Using the optical measurement techniques PIV and BOS and flow simulations using UPM, the aerodynamic mechanisms underlying the acoustic sources were revealed. The main results are summarized as follows:

- In hover, the tonal noise of the rotor dominates. The emission of broadband noise is strongest at the trailing edge of the rotor blade at 80% of the rotor radius. This shows that trailing edge noise is the dominant generation mechanism of broadband noise in the frequency range 1–8 kHz for the rotor under investigation. The intensity scales with the local flow velocity V^6.
- In forward flight, the sound emission is strongly dependent on the inflow velocity and the rotor tilt angle. As the tilt angle increases from 0°, a C-shaped sound emitting

area is created in the front half of the rotor disk. The visualization of the blade tip vortices with BOS and the simulation of the rotor wake with UPM demonstrate that the sound is generated by the interaction of the blade tip vortices in the rotor wake with the subsequent rotor blades.
- If the rotor has a tilt angle of +10°, two broadband sound generation areas emerge on the advancing and retreating sides of the rotor as the inflow velocity increases. PIV measurements in the rotor downwash and simulations of the vortex structure with UPM have shown that these source areas are associated with the roll up of super vortices on both sides of the rotor.

Up to now, the acoustic measurements at the RTG have been carried out on single rotors. After completing the experiments with single rotors, the test rig was extended to four rotors and aerodynamic experiments were carried out on the multicopter configuration [43]. Acoustic experiments on the multicopter configuration with the microphone array will follow. For this purpose, the acoustic quality of the RTG was improved by installing acoustic absorbers.

The presented results indicate that interactions between the blade wake and blade tip vortices with the subsequent rotor blades can also occur in small rotors during descent flight and have a significant impact on noise emission of multicopters. The noise emissions resulting from these effects can be mitigated through operational procedures by avoiding the regions of the flight envelope where such interactions take place. To the authors' knowledge, there are no publications to date that address the impact of operational procedures on the noise emissions of multicopters.

Appendix

See Fig. 20 and Table 1.

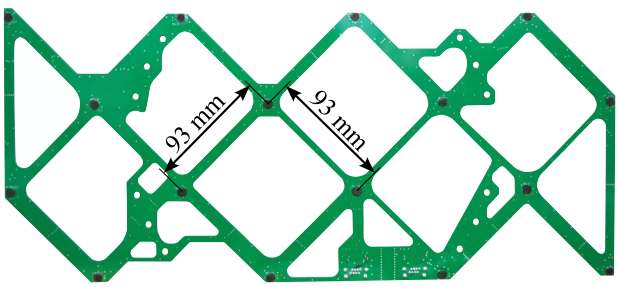

Fig. 20 Circuit board of the microphone array with 16 MEMS microphones

Table 1 Specifications of the cameras used in the BOS and PIV experiments

Camera	Sensor size	Focal length
Phantom VEO 640 L	2560 px × 1600 px	135 mm
PCO.edge 5.5 CMOS	2560 px × 2160 px	35 mm

Acknowledgements This research was funded by the DLR Project URBAN-Rescue, with funding from the German federal ministry for economic affairs and climate action (BMWK). The authors would like to thank Markus Krebs for his help during the preparation and execution of the experiments.

Funding Open Access funding enabled and organized by Projekt DEAL.

Data availability The presented data are accessible upon request, by contacting the corresponding author.

Declarations

Competing interest The authors declare that they have no conflict of interest.

References

1. Shaheen, S., Cohen, A., Farrar, E.: The potential societal barriers of urban air mobility (UAM). Natl Aeronaut Space Admin (2018). https://doi.org/10.7922/G28C9TFR
2. Cohen, A.P., Shaheen, S.A., Farrar, E.M.: Urban air mobility: history, ecosystem, market potential, and challenges. IEEE Trans Intell Trans Syst **22**(9), 6074–6087 (2021). https://doi.org/10.1109/TITS.2021.3082767
3. Greenwood, E., Brentner, K.S., Rau, R.F., Ted Gan, Z.F.: Challenges and opportunities for low noise electric aircraft. Int J Aeroacoust **21**(5–7), 315–381 (2022). https://doi.org/10.1177/1475472X221107377
4. Ramasamy, M., Leishman, J.G.: A Reynolds number-based blade tip vortex model. J Am Helic Soc **52**(3), 214–223 (2007)
5. Winslow, J., Otsuka, H., Govindarajan, B., Chopra, I.: Basic understanding of airfoil characteristics at low Reynolds numbers (10^4-10^5). J Aircr **55**(3), 1050–1061 (2018). https://doi.org/10.2514/1.C034415
6. Miller, M. A., Karli, G., Rahman, Z., Kandias, C., Greenwood, E., Palacios, J.: Characterizing rotor performance changes with scale in compressed air, 80th Annual Vertical Flight Society Forum and Technology Display, Montreal, QC, Canada, May 7–9, (2024)

7. Ning, Z., Hu, H.: An experimental study on the aerodynamics and aeroacoustic characteristics of small propellers, 54th AIAA Aerospace Sciences Meeting, San Diego, CA, USA, January 4–8, (2016)
8. Yang, Y., Liu, Y., Li, Y., Arcondoulis, E., Wang, Y.: Aerodynamic and aeroacoustic performance of an isolated multicopter rotor during forward flight. AIAA J **58**(3), 1171–1181 (2020). https://doi.org/10.2514/1.J058459
9. Gojon, R., Jardin, T., Parisot-Dupuis, H.: Experimental investigation of low Reynolds number rotor noise. J Acoust Soc Am **149**(6), 3813–3829 (2021). https://doi.org/10.1121/10.0005068
10. Zhou, W., Ning, Z., Li, H., Hu, H.: An experimental investigation on rotor-to-rotor interactions of small UAV propellers, 35th AIAA Applied Aerodynamics Conference, Denver, CO, USA, June 5–9, (2017)
11. Zawodny, N. S., Boyd, D. D., Burley, C. L.: Acoustic characterization and prediction of representative, small-scale rotary-wing unmanned aircraft system components, 72nd American Helicopter Society Annual Forum and Technology Display, West Palm Beach, FL, USA, May 16–19, (2016)
12. Kostek, A. A., Lößle, F., Wickersheim, R., Keßler, M., Boisard, R., Reboul, G., Gardner, A. D.: Experimental investigation of UAV rotor aeroacoustics and aerodynamics with computational cross-validation. CEAS Aeronaut J (2023), pp 1–16. https://doi.org/10.1007/s13272-023-00680-z
13. Mankbadi, R.R., Afari, S.O., Golubev, V.V.: High-fidelity simulations of noise generation in a propeller-driven unmanned aerial vehicle. AIAA J **59**(3), 1020–1039 (2021)
14. Yin, J., Rossignol, K., Rottmann, L., Schwarz, T.: Numerical studies on small rotor configurations with validation using acoustic wind tunnel data, CEAS Aeronaut J (2023), pp 1–32
15. Li, S., Lee, S.: Predictions and validations of small-scale rotor noise using ucd-quietfly, VFS Aeromechanics for Advanced Vertical Flight Technical Meeting, San Jose, CA, USA, January 25–27, (2022)
16. Grande, E., Romani, G., Ragni, D.: Aeroacoustic investigation of a propeller operating at low Reynolds numbers. AIAA J **60**(2), 860–871 (2022). https://doi.org/10.2514/1.J060611
17. Arcondoulis, E., Doolan, C., Zander, A. C.: Airfoil noise measurements at various angles of attack and low Reynolds number, Acoustics, Adelaide, SA, Australia, November 23–25, (2009)
18. Yakhina, G., Roger, M., Moreau, S., Nguyen, L., Golubev, V.: Experimental and analytical investigation of the tonal trailing-edge noise radiated by low Reynolds number aerofoils. Acoustics **2**(2), 293–329 (2020)
19. Leslie, A., Wong, K. C., Auld, D.: Broadband noise reduction from a mini-UAV propeller through boundary layer tripping, Annual Conference of the Australian Acoustical Society, Geelong, VIC, Australien, November 24–26, (2008)
20. Romani, G., Grande, E., Avallone, F., Ragni, D., Casalino, D.: Performance and noise prediction of low-Reynolds number propellers using the Lattice-Boltzmann method. Aerosp Sci Technol **125**, (2022). https://doi.org/10.1016/j.ast.2021.107086
21. Nardari, C., Casalino, D., Polidoro, F., Coralic, V., Brodie, J., Lew, P.: Numerical and experimental investigation of flow confinement effects on UAV rotor noise, 25th AIAA/CEAS Aeroacoustics Conference, Delft, The Netherlands, May 20–23, (2019). https://doi.org/10.2514/6.2019-2497
22. Thurman, C., Zawodny, N. S., Pettingill, N. A., Lopes, L. V., Baeder, J. D.: Physics-informed broadband noise source identification and prediction of an ideally twisted rotor, AIAA SciTech 2021 Forum, Orlando, FL, USA, January 8–12, (2021)
23. Pettingill, N. A., Zawodny, N. S.: Identification and prediction of broadband noise for a small quadcopter, 75th Annual Forum and Technology Display, Philadelphia, PA, USA, May 13–16, (2019)
24. Burley, C.L., Brooks, T.F.: Rotor broadband noise prediction with comparison to model data. J Am Helic Soc **49**(1), 28–42 (2004)
25. Brooks, T.F., Burley, C.L.: Blade wake interaction noise for a main rotor. J Am Helic Soc **49**(1), 11–27 (2004). https://doi.org/10.4050/JAHS.49.11
26. Yu, Y.H.: Rotor blade-vortex interaction noise. Progr Aerosp Sci **36**(2), 97–115 (2000). https://doi.org/10.1016/S0376-0421(99)00012-3
27. Romani, G., Casalino, D.: Rotorcraft blade-vortex interaction noise prediction using the Lattice-Boltzmann method. Aerosp Sci Technol **88**, 147–157 (2019). https://doi.org/10.1016/j.ast.2019.03.029
28. Chen, M., Hua, J., Maier, N., Burdette, D.: Acoustic measurements in single-rotor/wing interaction at low disk loading and Reynolds number. Int J Aeroacoust **23**(1–2), 20–37 (2024). https://doi.org/10.1177/1475472X231225630
29. Chen, M., Chen, Y., Hua, J., Maier, N., Burdette, D.: Experimental assessment of blowing effect on vehicle performance and aeroacoustics in small-rotor/wing interaction. J Vib Contr **31**(5–6), 966–980 (2025). https://doi.org/10.1177/10775463241236303
30. Lößle, F., Kostek, A., Schwarz, C., Schmid, R., Gardner, A., Raffel, M.: Aerodynamics of small rotors in hover and forward flight, 48th European Rotorcraft Forum, Winterthur, Switzerland, September 6–8, (2022)
31. Lößle, F.: Experimentelle Untersuchung der Aerodynamik und Aeroakustik kleiner Rotoren im Schwebe- und Vorwärtsflug, Ph.D. thesis, Leibniz University Hannover, (2024). https://doi.org/10.57676/me6e-j853
32. Seiferth, R.: Vorausberechnung und Beseitigung der Schwingungen von Freistrahl-Windkanälen, Monographien über Fortschritte der deutschen Luftfahrtforschung seit 1939, Aerodynamische Versuchsanstalt Göttingen, (1946)
33. Ernst, D., Geisler, R., Kleindienst, T., Ahlefeldt, T., Spehr, C.: Portable 512 MEMS-microphone-array for 3D-intensity-and beamforming-measurements using a FPGA based data-acquisition-system, 8th Berlin Beamforming Conference, Berlin, Germany, March 2–3, (2020)
34. Sijtsma, P.: Acoustic beamforming for the ranking of aircraft noise, Tech. rep., National Aerospace Laboratory NLR, TP-2012-137, (2012)
35. Sijtsma, P., Oerlemans, S., Holthusen, H.: Location of rotating sources by phased array measurements, 7th AIAA/CEAS aeroacoustics conference and exhibit, Maastricht, The Netherlands, May 28–30, (2001)
36. Raffel, M.: Background-oriented schlieren (BOS) techniques. Exp Fluids **56**(3), 1–17 (2015). https://doi.org/10.1007/s00348-015-1927-5
37. Schwarz, C., Bauknecht, A., Wolf, C.C., Coyle, A., Raffel, M.: A full-scale rotor-wake investigation of a free-flying helicopter in ground effect using BOS and PIV. J Am Helic Soc **65**(3), 1–20 (2020). https://doi.org/10.4050/JAHS.65.032007

38. Yin, J., Ahmed, S. R.: Treatment of unsteady rotor aerodynamics, Technical Report. IB 129-94/21, German Aerospace Center (DLR), (1994)
39. Ahmed, S.R., Vidjaja, V.T.: Unsteady panel method calculation of pressure distribution on BO 105 model rotor blades. J Am Helic Soc **43**(1), 47–56 (1998). https://doi.org/10.4050/JAHS.43.47
40. Winckelmans, G.S., Leonard, A.: Contributions to vortex particle methods for the computation of three-dimensional incompressible unsteady flows. J Comput Phys **109**(2), 247–273 (1993). https://doi.org/10.1006/jcph.1993.1216
41. Eppler, R.A., Somers, D.M.: A computer program for the design and analysis of low-speed airfoils. Technical report, NASA Technical Memorandum (1980)
42. Drela, M., Giles, M.B.: Viscous-inviscid analysis of transonic and low Reynolds number airfoils. AIAA J **25**(10), 1347–1355 (1987). https://doi.org/10.2514/3.9789
43. Kostek, A.A., Braukmann, J.N., Lößle, F., Miesner, S., Visingardi, A., Boisard, R., Riziotis, V., Keßler, M., Gardner, A.D.: Experimental and computational investigation of aerodynamic interactions in quadrotor configurations. J Am Helic Soc **69**, 1–17 (2024). https://doi.org/10.4050/JAHS.69.022009
44. Ffowcs Williams, J.E., Hall, L.H.: Aerodynamic sound generation by turbulent flow in the vicinity of a scattering half plane. J Fluid Mech **40**(4), 657–670 (1970). https://doi.org/10.1017/S0022112070000368
45. Ghee, T.A., Elliott, J.W.: The wake of a small-scale rotor in forward flight using flow visualization. J Am Helic Soc **40**(3), 52–65 (1995). https://doi.org/10.4050/JAHS.40.52
46. Tan, J., Wang, H.: Simulating unsteady aerodynamics of helicopter rotor with panel/viscous vortex particle method. Aerosp Sci Technol **30**(1), 255–268 (2013). https://doi.org/10.1016/j.ast.2013.08.010